

Emission and afterglow properties of an expanding RF plasma with nonuniform neutral gas density

Vernon H. Chaplin and Paul M. Bellan

Citation: *Physics of Plasmas* **23**, 083506 (2016); doi: 10.1063/1.4960326

View online: <http://dx.doi.org/10.1063/1.4960326>

View Table of Contents: <http://scitation.aip.org/content/aip/journal/pop/23/8?ver=pdfcov>

Published by the [AIP Publishing](#)

Articles you may be interested in

[Absolute and relative emission spectroscopy study of 3 cm wide planar radio frequency atmospheric pressure bio-plasma source](#)

Appl. Phys. Lett. **107**, 053702 (2015); 10.1063/1.4928470

[Measurement and modeling of neutral, radical, and ion densities in H₂-N₂-Ar plasmas](#)

J. Appl. Phys. **117**, 083303 (2015); 10.1063/1.4913623

[Neutral depletion and the helicon density limit](#)

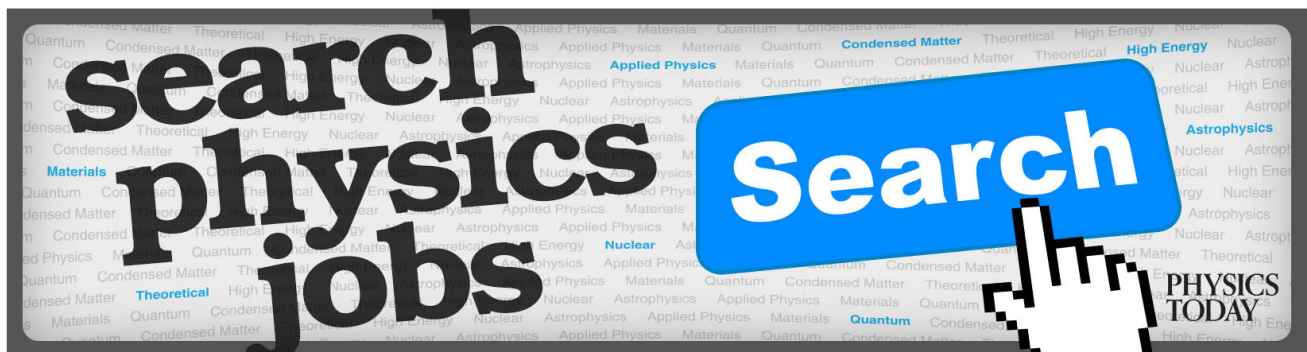
Phys. Plasmas **20**, 123511 (2013); 10.1063/1.4849376

[Neutral argon density profile determination by comparison of spectroscopic measurements and a collisional-radiative model \(invited\)](#)

Rev. Sci. Instrum. **77**, 10F304 (2006); 10.1063/1.2219440

[Determination of negative ion density with optical emission spectroscopy in oxygen afterglow plasmas](#)

Appl. Phys. Lett. **72**, 2391 (1998); 10.1063/1.121394



Emission and afterglow properties of an expanding RF plasma with nonuniform neutral gas density

Vernon H. Chaplin and Paul M. Bellan

Applied Physics and Materials Science Department, California Institute of Technology, Pasadena, California 91125, USA

(Received 27 March 2016; accepted 21 July 2016; published online 5 August 2016)

We describe some notable aspects of the light emission and afterglow properties in pulsed, high-density (10^{18} – 10^{20} m⁻³) argon inductively coupled discharges initiated following fast gas injection. The plasma was created in a long, narrow discharge tube and then expanded downstream of the radiofrequency (RF) antenna into a large chamber. Fast camera images of the expanding plasma revealed a multi-phase time-dependent emission pattern that did not follow the ion density distribution. Dramatic differences in visible brightness were observed between discharges with and without an externally applied magnetic field. These phenomena were studied by tracking excited state populations using passive emission spectroscopy and are discussed in terms of the distinction between ionizing and recombining phase plasmas. Additionally, a method is presented for inferring the unknown neutral gas pressure in the discharge tube from the time-dependent visible and infrared emission measured by a simple photodiode placed near the antenna. In magnetized discharges created with fast gas injection, the downstream ion density rose by $\Delta n_i \sim 10^{18}$ m⁻³ in the first ~ 100 μ s after the RF power was turned off. The conditions conducive to this afterglow density rise are investigated in detail, and the effect is tentatively attributed to pooling ionization. *Published by AIP Publishing.*

[<http://dx.doi.org/10.1063/1.4960326>]

I. INTRODUCTION

Pulsed, partially ionized gas discharges have important applications in materials processing,¹ chemical sample analysis,² and other research fields and industries. Advantages of pulsed operation include the ability to obtain high plasma densities without excessive heat loads on the system³ and opportunities to take advantage of the unique properties of the “afterglow” plasma that remains after the power source is switched off, such as high plasma density (n_i) with very low electron temperature (T_e)³ and intense visible and infrared (IR) light emission.⁴

In this paper, we discuss some interesting properties of the emission characteristics and afterglow evolution in a high density (peak $n_i \gg 10^{19}$ m⁻³) pulsed radiofrequency (RF) discharge at 100–700 mTorr. Argon gas was transiently injected into a high aspect ratio cylindrical discharge tube surrounded by an RF antenna, which ionized the gas and inductively deposited ≤ 3 kW of 13.56 MHz RF power for pulse lengths of 100–1000 μ s. The plasma diffused out of the tube and expanded into a larger vacuum chamber (see Fig. 1), where it was used to seed ionization in the Caltech Magnetohydrodynamically (MHD)-Driven Jet Experiment, a pulsed power experiment that simulates astrophysical accretion disk jets.⁵

The properties of the RF plasma were highly dependent on the neutral gas density n_{Ar} in the long, narrow discharge tube at the time when the discharge was initiated,⁶ but this density could not be easily measured with a fast ion gauge (Ref. 7, Appendix B.1) due to restricted physical access to the region of interest (see Fig. 1). Fortunately, a method was discovered for indirectly determining n_{Ar} by comparing the time-dependent visible and IR light emission from

discharges formed using fast gas injection to the emission obtained with a known uniform argon fill pressure (P_{Ar}). This technique, described in Sec. IV, enabled accurate values of n_{Ar} to be determined for use in numerical models of the experiment.⁶

The expansion of the RF plasma out of the tube was monitored with a fast intensified charge-coupled device (ICCD) camera in order to optimize the trigger timings for the pulsed power experiment. The image time series (see Sec. V) appeared to show a complex multi-phase expansion process in which the plasma emerged from the tube, retreated, and then appeared again after the RF power was turned off. However, Langmuir probe measurements showed that these observations were highly deceptive, because the brightness detected by the camera was poorly correlated with the local plasma density. Due to the existence of several different regimes for atomic processes producing visible and IR line emission in a partially ionized plasma, the discharge could be dim in the regions where n_i was high and bright in regions where there were mostly neutrals present. This result is of significant importance for a variety of laboratory plasma experiments because imaging diagnostics are widely used to characterize plasma dynamics. For example, high-speed cameras have been used to track MHD-driven plasma jets,⁸ to characterize fluctuation modes in linear plasma columns⁹ and Hall thrusters,¹⁰ and to diagnose fusion edge plasmas.¹¹ Hollow cathode modes of operation are characterized by the “spot” or “plume” emission structure that is visible downstream of the orifice (Ref. 12, Section 6.10), and the presence of a tail of emission bending away from the machine axis in Hall thrusters has been assumed to correlate with the direction of electron flow leaving the cathode.¹³

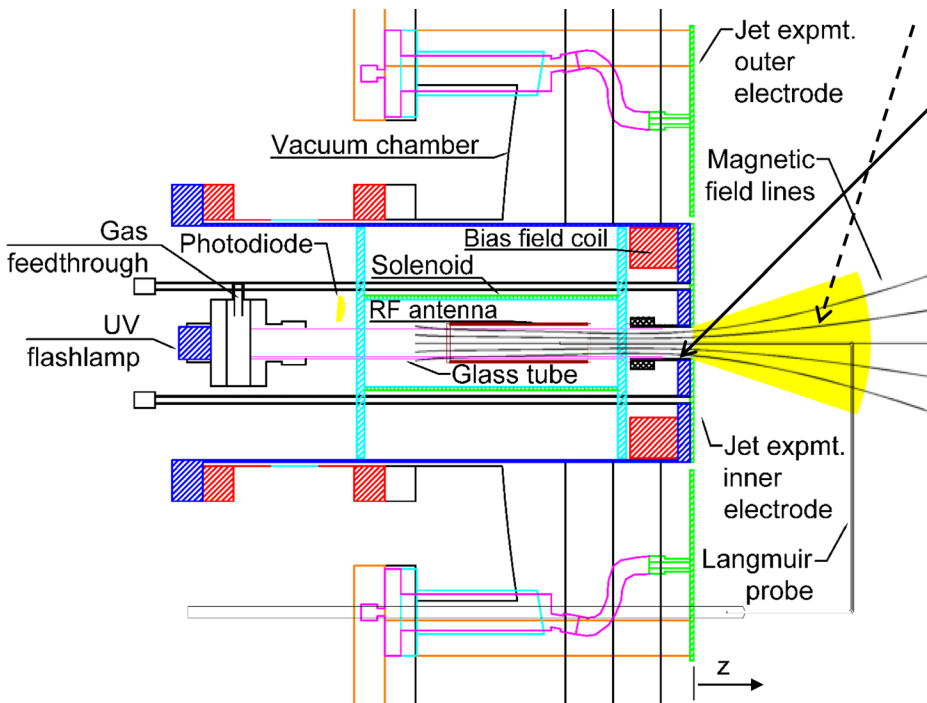


FIG. 1. Side-on cross-sectional view of the RF discharge tube and coaxial electrodes on the Caltech MHD-Driven Jet Experiment (Adapted from Rev. Sci. Instrum. **86**, 073506 (2015). Copyright 2015 AIP Publishing LLC). The cable leading to the RF antenna and some other minor hardware elements have been omitted for clarity. As illustrated in the figure, plasma created inside the antenna expanded into the main vacuum chamber, where it was used to seed ionization of additional neutral gas in the pulsed power experiment. Arrows show the lines of sight for spectroscopy (solid line) and for the fast camera (dotted line).

While it is well known that the visible emissivity of a plasma is a function of n_e , T_e , and n_{gas} and does not necessarily scale directly with n_e ,¹¹ the drastic qualitative discrepancy between the gross plasma dynamics and the observed light emission in our experiment is noteworthy. Several aspects of the plasma properties made the experiment unique and allowed for complex atomic physics. The high density of RF power input (>2 kW into a 2.2 cm inner diameter discharge tube) led to an unusually high plasma density for an inductively coupled discharge in this pressure range; as a result, stepwise ionization dominated over direct ionization from the ground state.^{6,14} The high population densities of ground state and excited neutral atoms made the plasma optically thick at the wavelengths of a number of important emission lines. Additionally, axial nonuniformity of the neutral gas density played an important role in regulating the time-dependent discharge evolution. We interpret our results in light of Fujimoto's theory of ionizing versus recombining phase plasmas,¹⁵ which shows that the light emission from bounded or time-varying laboratory plasmas can differ substantially from equilibrium predictions.

Although the apparent complexity of the plasma expansion process suggested by the camera images was not corroborated by Langmuir probe measurements, the probe did confirm one unexpected feature: a dramatic rise in n_i downstream of the source region following RF power turn-off under some conditions (see Sec. VI). This phenomenon has been observed in other noble gas discharges at similar pressures^{16–18} and has been attributed to metastable-metastable (pooling) ionization. In several cases, an afterglow density increase has been observed in helium plasmas but not in argon;^{17,19} in contrast, we observed a strong effect in argon discharges, but only when the background gas density was nonuniform and a magnetic field was applied. The magnitude of the density increase ($\Delta n_i \sim 10^{18} \text{ m}^{-3}$) in our experiment

was at least 10–100 times larger than those seen previously. Experiments in which hydrogen gas was added to the chamber supported the notion that pooling ionization was responsible for the afterglow density rise; however, the timescale for quenching of argon metastables by electron impacts may have been too short for this process to fully account for the observed Δn_i .

II. EXPERIMENT OVERVIEW

Details of the experiment setup and motivation have been described previously,¹⁴ and only a brief overview of the apparatus will be given here. A custom battery-powered 3 kW 13.56 MHz RF amplifier was used to drive a 10.5 cm long half-turn helical antenna²⁰ surrounding the $R = 1.1$ cm inner radius quartz tube shown in Fig. 1, creating a high-density plasma that expanded out of the tube into the main vacuum chamber. In the usual configuration, the nearest end of the antenna was located 5.9 cm behind the plane of the jet experiment electrodes, which we define to be at $z = 0$ cm. The RF amplifier was pulsed for 0.1–1 ms, and a xenon arc UV flashlamp (Excelitas Technologies model FX-1165) was triggered at the time of RF turn-on in order to provide seed ionization and improve the reproducibility of the discharge.

Prior to initiating the discharge, a background magnetic field was applied using the solenoid and 100-turn “bias field coil” shown in the figure, providing radial confinement of the expanding RF plasma and setting up an astrophysically relevant dipole-like configuration at $z > 0$. The field was approximately constant on the timescale of the discharge, with a typical magnitude of 600–1000 Gauss at $(r, z) = (0, 0)$. The field strength could be adjusted by varying the charging voltages for the capacitor banks driving current through the coils—the standard values used were $V_{bias} = 80$ V for the bias field coil and $V_{sol.} = 60$ V for the solenoid.

Argon gas was transiently injected at the rear end of the discharge tube using a fast pulsed gas valve. The trigger timing and charging voltage for the capacitor bank powering the gas valve could be adjusted to change the amount of gas present at the time of RF turn-on (defined as $t = 0 \mu\text{s}$), but the detailed pressure distribution in the discharge tube was not known. Based on the room temperature sound speed for argon, the gas travel time from the valve to $z = 0$ was estimated to be 5.6 ms, and the gas valve was triggered at $t_{\text{gas}} = -6.0 \text{ ms}$ unless otherwise noted. Pulsed gas injection was necessary for the MHD-driven jet experiment in order to have a sufficient quantity of gas in the vicinity of the electrodes for plasma breakdown, while allowing the jet to propagate into vacuum after its formation.

III. DIAGNOSTICS

The RF discharge properties were diagnosed using a cylindrical single Langmuir probe with radius $r_{\text{probe}} = 2.6 \times 10^{-4} \text{ m}$ and surface area $A_{\text{probe}} = 4.5 \times 10^{-6} \text{ m}^2$ that could access the regions both inside and outside the discharge tube ($-9 \text{ cm} \leq z \leq 9 \text{ cm}$), as shown in Fig. 1. All measurements presented in this paper were taken along the central axis of the chamber ($r = 0$). The probe did not have RF compensation and thus was used only to measure ion saturation current (I_{sat}), except in the afterglow, when the full I-V curve could be analyzed. Because the gas pressure inside the discharge tube was $>100 \text{ mTorr}$ for these experiments (see Sec. IV), ion-neutral collisions in the pre-sheath reduced the I_{sat} collected by the probe to below the value predicted by collisionless theories, and the magnitude of the ion density n_i inside the tube could not be calculated accurately.²¹ However, for experiments at a given gas pressure, the measured I_{sat} still scaled linearly with n_i , so using I_{sat} measurements to track temporal variations in density or compare densities between different discharges was a valid approach, as long as the effect of variations in T_e could be neglected.

A Cooke Corporation 12-bit ICCD camera with a Nikon f/1.4 lens was used to photograph the visible and IR light emission in the main vacuum chamber (see Fig. 1). Typically, $10 \mu\text{s}$ exposure time was used. The RF discharge was extremely reproducible, so a sequence of images taken during successive shots could be combined to effectively create a movie of the plasma expansion. For all images presented in this paper, false color is used to indicate overall light intensity, with the brightest regions shown in white and dimmer areas in red.

A photodiode (United Detector Technology PIN-10DP) was installed at the rear of the discharge tube, as shown in Fig. 1, to monitor the overall time-dependent visible and near infrared emission from the antenna region. The incident light was attenuated so that the photodiode remained in the linear regime, with photocurrent below $\sim 5 \text{ mA}$.

More detailed information about the populations of excited atoms and ions during the main discharge and afterglow was obtained from passive emission spectroscopy. Collisional-radiative (CR) modeling of the argon plasma was not attempted, but useful qualitative conclusions could still be drawn from the relative values of various line intensity

ratios, as discussed in Sec. V. An optical fiber attached to a collimating lens viewed the discharge tube aperture through a window on the main vacuum chamber, collecting light along a $<1 \text{ cm}$ diameter line of sight passing through the point $(r, z) = (0, 0)$ (see Fig. 1). Further out in the expanding plasma plume, the emission intensity was too weak to reproducibly measure time-resolved line ratios. Light collected by the fiber was coupled into a Jarrell-Ash 82-092 0.5 m Ebert scanning spectrometer, which was operated as a monochromator with a Hamamatsu R928 photomultiplier tube (PMT) used as a detector. Intensity calibration of the spectroscopic system was not essential because only qualitative trends in the line ratios were of interest; nevertheless, the measured line ratios were corrected for the known wavelength-dependent quantum efficiency of the PMT.

IV. NEUTRAL GAS PRESSURE ESTIMATE FROM TIME-DEPENDENT EMISSION INTENSITY

The visible and IR emission from the RF discharge was a strong function of the gas pressure in the narrow tube, which in turn depended nonlinearly on the charging voltage of the capacitor bank powering the fast gas valve.²² In Fig. 2(a), we show the total time-dependent emission measured by the photodiode at the rear of the discharge tube during discharges with the RF power on for $200 \mu\text{s}$, for a range of gas bank voltages from 450 V to 700 V. The discharge was very bright at early times due to the elevated electron temperature and high neutral argon excited state populations,⁶ and then it dimmed and approached a steady state brightness from $t = 100\text{--}200 \mu\text{s}$. When the RF power was turned off at $t = 200 \mu\text{s}$, the emission declined rapidly as T_e decreased and electron-impact excitation ceased, but at higher gas bank voltages, it rose again a few μs later, exhibiting a strong afterpeak.

Similar trends were observed during experiments with a uniform argon gas pressure in the chamber, as shown in Fig. 2(b). In fact, as illustrated in Fig. 3, an extremely close correspondence existed between the magnitude and time dependence of the photodiode signal obtained at a given fast gas valve bank voltage and the signal recorded at some uniform gas pressure. The match between the measured emission patterns was so precise that the plasma conditions, and in particular, the argon gas pressure, must have been nearly identical between the pairs of shots shown in Fig. 3. Therefore, we may interpret the time-dependent visible and IR emission as giving an indirect measurement of the pressure produced in the discharge tube by the fast gas valve.

At low gas bank voltages, the correspondence between the emission produced during experiments with the fast gas valve and during uniform pressure experiments was nearly exact at all times (Fig. 3(a)), while at higher bank voltages a somewhat different uniform pressure was needed to match the emission during the main discharge period versus during the afterglow (Figs. 3(b) and 3(c)). A plausible explanation involves re-absorption of line emission. The line center absorption cross section for a Doppler-broadened emission line²³ is

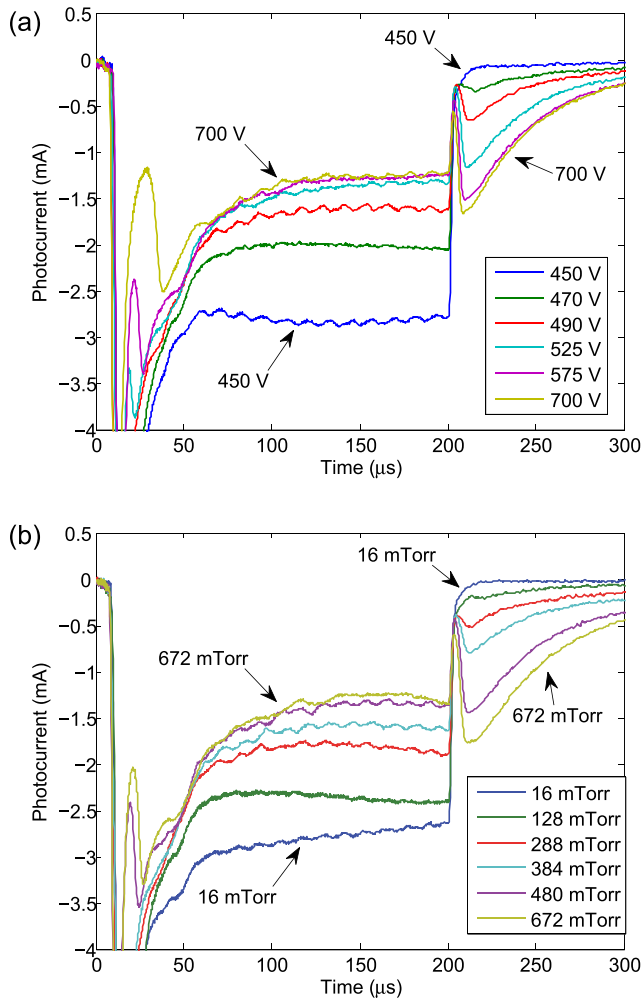


FIG. 2. Photodiode signals during magnetized discharges ($V_{bias} = 80$ V, $V_{sol.} = 0$ V) with the RF power on from $t = 0$ – 200 μ s. Similar results were obtained with $B = 0$. The photocurrent was always negative, with its magnitude proportional to the incident brightness. (a) Data from experiments with the fast gas valve used (the legend shows the gas bank voltage V_{gas}), and (b) data from experiments with a uniform pressure in the discharge tube.

$$\sigma_{\lambda_0} \approx \frac{\lambda_0^3}{8\sqrt{2}\pi^{3/2}} \frac{g_p}{g_q} A_{pq} \sqrt{\frac{M}{k_B T_{gas}}}, \quad (1)$$

where A_{pq} is the spontaneous transition rate from the upper energy level p to the lower level q ,²⁴ g_p and g_q are the statistical weights of these levels, and $M = 6.7 \times 10^{-26}$ kg for argon. Numerical simulations of discharges at $P_{Ar} \leq 300$ mTorr (Ref. 6) (Ref. 25, Section 5.1) have shown that the population densities inside the RF antenna of each of the neutral argon (Ar I) $4s$ excited states were on the order of 10^{18} m^{-3} during the quasi-steady state period of the discharge. Taking the specific example of the Ar I 696.5 nm line, which is produced by a $4p \rightarrow 4s$ transition and is one of the strongest visible emission lines in the plasma, and assuming $T_{gas} = 0.05$ eV, we find $\sigma_{\lambda_0} \approx 6 \times 10^{-17}$ m^2 . Thus, the absorption mean free path for this line was $l_{mfp} = (n_q \sigma_{\lambda_0})^{-1} \sim 2$ cm, which is smaller than the length of the discharge tube, so the photodiode was not able to collect much light from the region near $z = 0$, while the RF power was on.

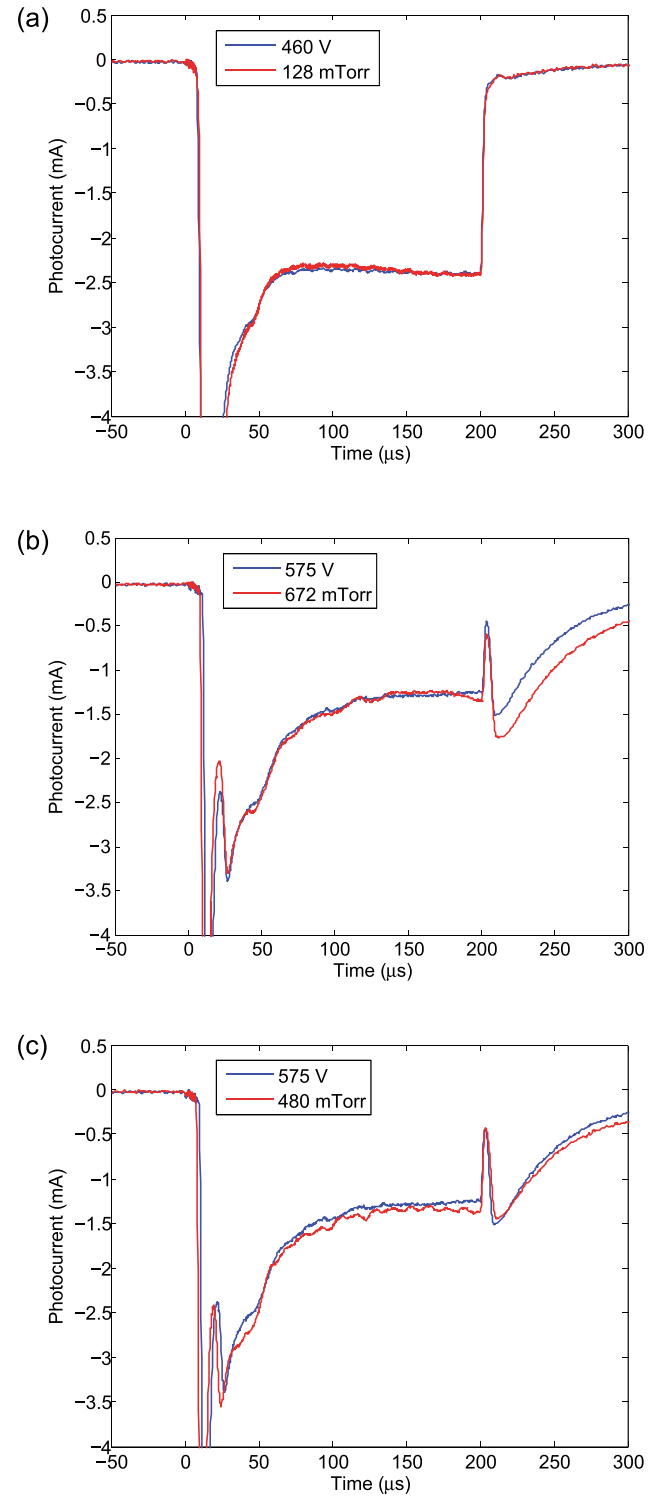


FIG. 3. Examples of the close correspondence between photodiode signals obtained during experiments with the fast gas valve used and with a uniform pressure in the discharge tube. (a) The time-dependence and brightness of the emission with a gas bank voltage $V_{gas} = 460$ V were closely reproduced with a uniform pressure of $P_{Ar} = 128$ mTorr. (b) and (c): For $V_{gas} = 575$ V, the best match to the emission during the RF on period ($t < 200$ μ s) was obtained with $P_{Ar} = 672$ mTorr, while the best match to the afterpeak brightness was obtained with $P_{Ar} = 480$ mTorr.

When the power was turned off, the population densities of the $4s$ states decreased rapidly⁶ (including the metastable states, which were rapidly depopulated by electron impacts due to the high density $n_e > 10^{19}$ m^{-3} inside the antenna).

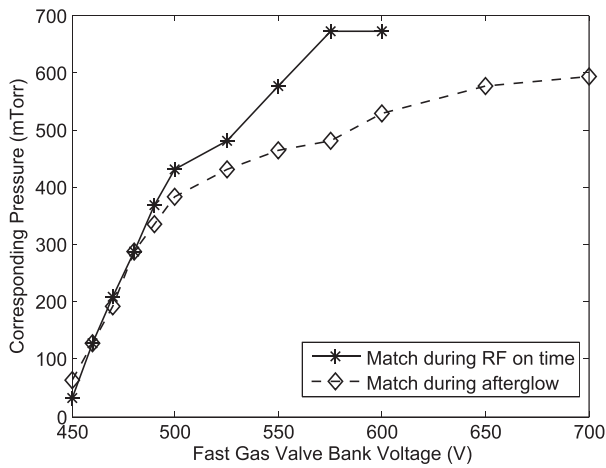


FIG. 4. Pressure in the discharge tube as a function of gas bank voltage, as determined from matching photodiode traces between experiments that used the fast gas valve and experiments that had uniform P_{Ar} . The two curves show the best fit pressure from emission comparisons during the RF on time (as in Fig. 3(b)) and in the afterglow (as in Fig. 3(c)).

Therefore, re-absorption became less important in the afterglow, and the photodiode could see deeper into the plasma. If there was a gas pressure gradient $\partial P_{Ar}/\partial z < 0$ when the fast gas valve was used (it is reasonable to expect that P_{Ar} was higher near the gas inlet than downstream near $z=0$), then most of the visible/IR photons collected by the photodiode during the main discharge would have originated from a region with relatively higher pressure than that in the region

producing the light collected during the afterglow, consistent with the trend in Figs. 3(b) and 3(c).

Fig. 4 shows the overall dependence of P_{Ar} on V_{gas} , as determined from photodiode measurements during the main discharge and during the afterglow. Since knowledge of the pressure toward the front of the discharge tube near the electrodes was of the most interest for interpreting the other experimental results, the pressure measurement using the afterglow emission was preferred. With the most commonly used gas bank voltage of $V_{gas} = 550$ V, the inferred pressure was $P_{Ar} \approx 460$ mTorr.

The pressure-measurement technique described here could be applied even though the detailed excited state population densities that produced the observed line emission were not known; in fact, the complexity of the emission processes was advantageous, as this made it very unlikely that a close match between the overall time-dependent emission patterns in two different discharges could have been obtained if the gas pressures were not equal. Nevertheless, the method should be validated in the future by comparisons with direct gas pressure measurements in an experiment with a more accessible geometry. If the validity of the approach is confirmed, it could be useful for inferring the gas pressure in other experiments that employ a fast gas valve to feed gas to an RF plasma source.²⁶

V. MOVIES OF RF PLASMA EXPANSION

In the usual experimental setup with the magnetic field coils turned on, fast camera movies of the plasma expansion

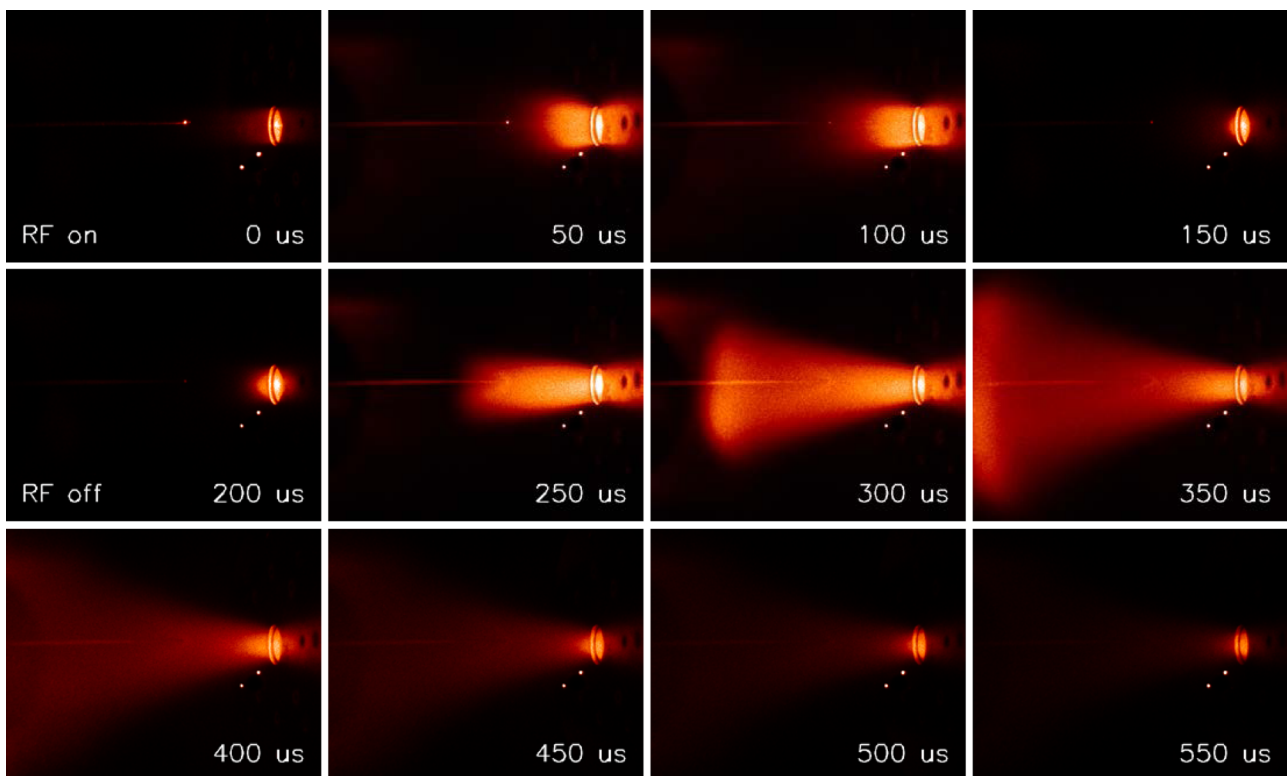


FIG. 5. Fast camera images of RF plasma expansion into the main vacuum chamber for shots with the RF power on for 200 μ s and the bias field coil and solenoid turned on. The orientation of the images is flipped with respect to the source schematic in Fig. 1—here the RF source tube and antenna are located to the right of the field of view. The Langmuir probe is visible along the chamber axis, and the probe tip at $z = 6$ cm can be seen glowing in the early frames. The two white dots located directly to the lower left of the discharge tube aperture are an artifact caused by a damaged portion of the ICCD detector.

into the main vacuum chamber comprised several distinct phases. Examples from discharges with the RF power on for $200\ \mu\text{s}$ and $400\ \mu\text{s}$ are shown in Figs. 5 and 6, respectively. At early times, there was a bright, expanding cloud of emission near the output of the discharge tube, but this dimmed at around $t = 150\ \mu\text{s}$. In Fig. 5, the RF source was turned off at $t = 200\ \mu\text{s}$, and subsequently, a cone of plasma appeared to expand in the chamber, roughly following the magnetic field lines shown in Fig. 1. On the other hand, when the RF power was left on until $t = 400\ \mu\text{s}$ (Fig. 6), very little visible/IR emission was detected from the region in front of the discharge tube output from $t = 200$ to $400\ \mu\text{s}$ —only after RF turn-off did an expanding cone of plasma appear. The images give the impression that the expansion of the plasma was somehow inhibited as long as the RF power remained on.

A different sequence was observed in experiments with the magnetic field coils turned off, as shown in Fig. 7. In this case, although the RF power remained on, an expanding region of emission was readily visible from $t = 150$ to $300\ \mu\text{s}$. This feature dimmed by $t = 350\ \mu\text{s}$, and after RF turn-off, a new expanding emitting region appeared; this was similar in character but dimmer than the corresponding region in Fig. 6. Additionally, the initial emitting region at $t \leq 100\ \mu\text{s}$ was much smaller in the unmagnetized case than with the magnetic field coils turned on.

These image series were suggestive of a multi-stage plasma expansion process that was far more complex than the expected steady field-aligned ambipolar diffusion. However, Langmuir probe measurements presented a very different picture of the expansion dynamics. Fig. 8 shows $I_{sat.}$ measured at $z = 6\ \text{cm}$ for the three scenarios corresponding to the images

in Figs. 5–7. In all three cases, the plasma density at this location was low for the first $200\ \mu\text{s}$ after RF turn-on and then rose rapidly to a peak between $t = 200$ and $300\ \mu\text{s}$. Despite the vast differences in visible brightness of the plasma plume at this time, the peak $I_{sat.}$ values were within 50% of one another. In two of the three cases, $I_{sat.}$ decreased monotonically after its initial peak; the third case, in which $I_{sat.}$ rose to a second peak $\sim 100\ \mu\text{s}$ after the power was turned off, will be discussed in Sec. VI.

It should be noted that the Langmuir probe measured $I_{sat.}$ locally on axis ($r = 0\ \text{cm}$), while the camera detected line-integrated emission. Thus, a precise correspondence between $I_{sat.}$ and brightness would not have been expected even if the emissivity were directly proportional to n_i . Fortunately, the cylindrical symmetry of the experiment and the nearly side-on viewing angle of the camera limited the ambiguity in comparisons of the images and probe data. Radial Langmuir probe scans, shown in Figure 6.22 of Ref. 25, confirmed that the density peaked on axis and showed that the plasma expanded radially only slightly more in experiments with $B = 0$ than in the magnetized case. Therefore, the line integration path length for imaging was similar for the three scenarios shown in Fig. 8, and it was straightforward to make qualitative comparisons between these $I_{sat.}$ measurements and the corresponding images.

The most obvious conclusion to be drawn from Figs. 5–8 is that the emissivity of the plasma was not proportional to the local ion density. This was already demonstrated in the photodiode data from Fig. 2, which showed that the quasi-steady state brightness in the discharge tube was lower at high P_{Ar} , while Langmuir probe measurements and numerical

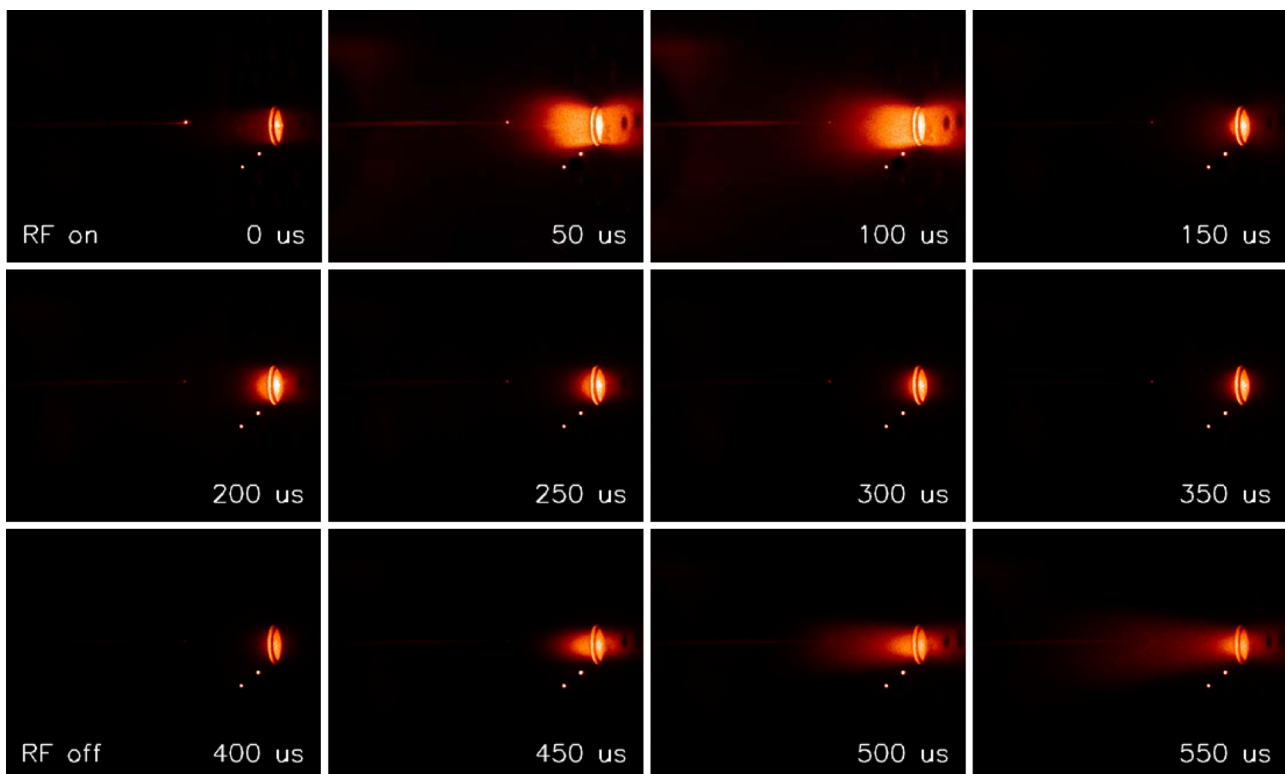


FIG. 6. Images of the RF plasma expansion for shots with the RF power on for $400\ \mu\text{s}$ and the bias field coil and solenoid turned on.

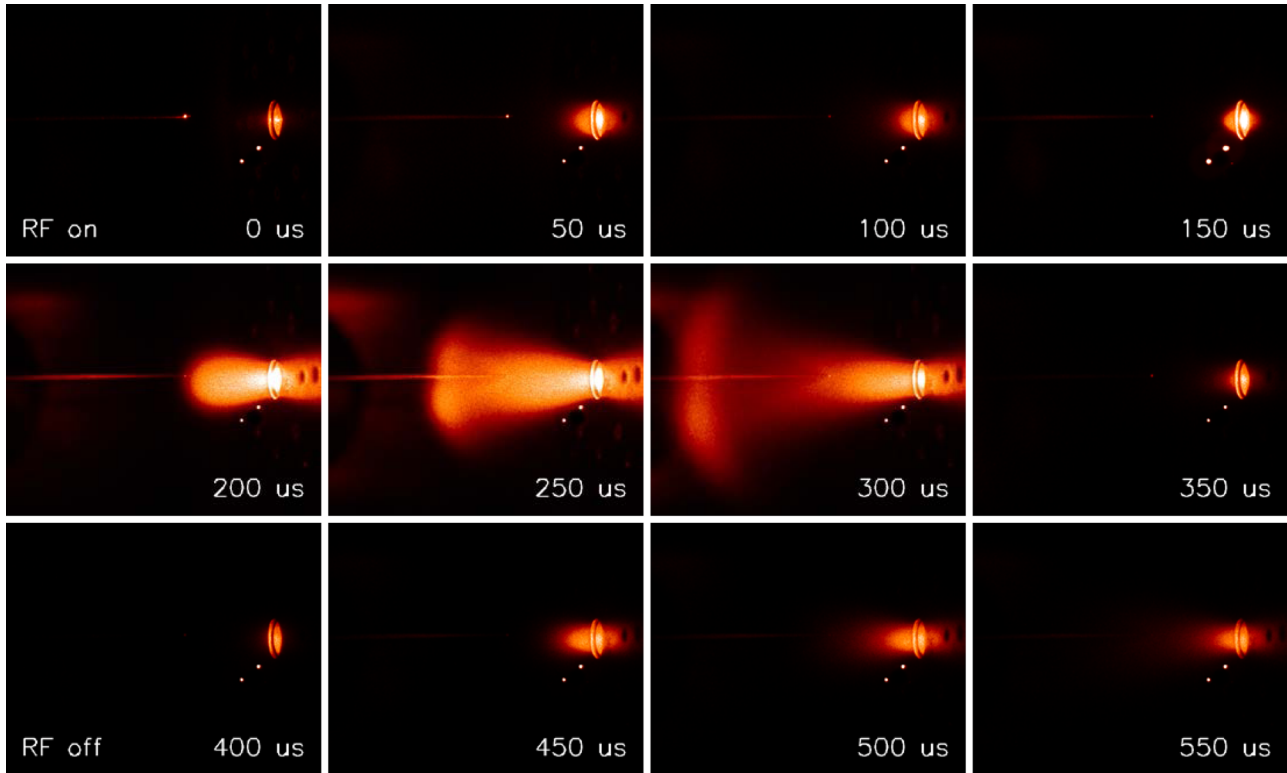


FIG. 7. Images of the RF plasma expansion for shots with the RF power on for 400 μs and the magnetic field coils turned off.

simulations⁶ have shown that the density increased with gas pressure. The discrepancy between the temporal evolution of the images and the probe data was more dramatic and begs for detailed physical explanation.

Consider first the initial interval of the discharge, from $t = 0$ to 150 μs . Fig. 8 shows that the plasma density out in the main chamber was low at this time, but there was still

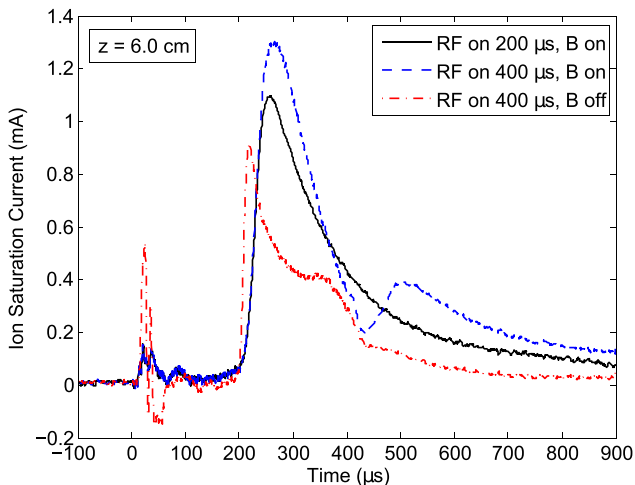


FIG. 8. Ion saturation current measured with $V_{probe} = -15.3$ V at $z = 6$ cm during the discharges photographed in Figs. 5–7. The negative current collected at $t = 20 - 60$ μs in the “RF on 400 μs , B off” case indicates that the probe was collecting some electron current at this time because the plasma was hotter than usual at the probe location; at later times, however, the current measured was expected to be truly ion saturation current, proportional to $n_i\sqrt{T_e}$. The electron temperature was expected to change drastically only immediately after RF turn-off—at other times, changes in I_{sat} should roughly correspond to variations in the plasma density.

bright emission visible at the probe location in Figs. 5 and 6. The cause of the emission was probably fast electrons streaming out of the antenna region and colliding with a pre-existing neutral gas cloud, exciting the argon atoms, which then produced line radiation. Evidence for this interpretation is provided by Fig. 9, which shows that the size of the bright region varied when the timing of neutral gas injection was adjusted between -4.5 ms and -6.5 ms: for longer fast gas valve delays, the neutral gas had propagated further into the chamber by $t = 0$ μs , and the emitting region was correspondingly larger. With no magnetic field, the fast electrons were not confined radially and few made it out of the source tube, explaining the smaller size of the initial emitting region in Fig. 7 compared to Figs. 5 and 6.

By the fourth frame of Figs. 5–7 ($t = 150$ μs), the initial cloud of emission had dimmed, even though RF power was still being delivered to the plasma. One plausible explanation for the dimming is that sufficient plasma density had built up near the front of the discharge tube to scatter the primary electrons accelerated by the antenna before they could reach the argon gas cloud out in the main chamber. The momentum transfer cross section (Ref. 27, p. 16) for a 10 eV electron colliding with lower energy thermal electrons is $\sigma_{ee} \sim 5 \times 10^{-18}$ m², so if the electron density was $n_e \sim 10^{19}$ m⁻³, then the momentum transfer mean free path for primary electrons was $\lambda_{ee} = (\sigma_{ee}n_e)^{-1} \sim 2$ cm, and the energy transfer mean free path was similar. At earlier times, the mean free path for electron-neutral collisions was already short ($\lambda_{en} \approx 7 \times 10^{-4}$ m at $P_{Ar} = 460$ mTorr (Ref. 1, Figure 3.13)), but the energy lost by the primary electrons in these collisions was negligible, so they still emerged from the

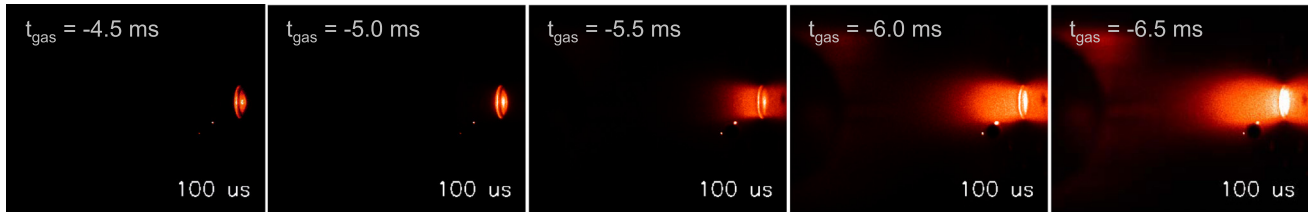


FIG. 9. Fast camera images of the emission in front of the source tube output at $t = 100 \mu\text{s}$ for five different fast gas valve delays. The bias field coil and the solenoid were turned on.

discharge tube with sufficient energy to collisionally excite argon atoms.

For all three of the experimental conditions shown in Figs. 5–7, the plasma density at $z = 6.0 \text{ cm}$ peaked between $t = 200$ and $300 \mu\text{s}$, yet a visible plasma was present at this location and time only in Figs. 5 and 7. Emission line intensity ratios measured with the spectrometer provide some clues regarding how to reconcile the images with the I_{sat} measurements. The main lines observed were Ar I 696.5 nm (electron transition: $4p \rightarrow 4s$; upper level energy $\equiv E_k = 13.36 \text{ eV}$; and transition rate $\equiv A_{ki} = 6.4 \times 10^6 \text{ s}^{-1}$) and Ar I 703.0 nm ($6s \rightarrow 4p$; $E_k = 14.88 \text{ eV}$; and $A_{ki} = 2.7 \times 10^6 \text{ s}^{-1}$).²⁴

The intensity I_{ki} of an emission line scales as $I_{ki} \propto n_k A_{ki}$, where A_{ki} is a property of the individual atom or ion and does not depend on the conditions in the plasma. Fujimoto¹⁵ showed that for any plasma, the population density of an energy level k in ionization stage j may be expressed as the sum of a term proportional to the ground state population density of the ion j and a term proportional to the ion density in the next ionization stage $j + 1$, i.e.,

$$n_k^j = Z_k^j \alpha_k^j n_1^{j+1} n_e + [Z_k^j / Z_1^j] \beta_k^j n_1^j, \quad (2)$$

where the ionization stage is labeled in the superscript and the energy level within the ion/atom is labeled in the subscript (a subscript 1 refers to the ground state). $\alpha_k^j(n_e, T_e)$ and $\beta_k^j(n_e, T_e)$ are temperature- and density-dependent coefficients that encapsulate the detailed atomic physics. $Z_k^j(T_e)$ is the Saha-Boltzmann coefficient

$$Z_k^j = \frac{g_k}{2g_1^j} \left(\frac{h^2}{2\pi m_e k_B T_e} \right)^{3/2} \exp\left(\frac{\chi^j - E_k}{k_B T_e} \right), \quad (3)$$

where χ^j is the ionization potential. A plasma in which the term involving β_k^j dominates is labeled an “ionizing” plasma, while a plasma in which the term containing α_k^j dominates is labeled a “recombining” plasma. These terms refer solely to the dominant mechanism populating the atomic energy levels and do not necessarily imply that the ionization balance of the plasma is changing in time. For example, many steady state laboratory plasmas are in the “ionizing” regime because recombination is negligible in comparison to charged particle losses to the walls.

The presence of the Saha-Boltzmann coefficient Z_k^j in both terms of Eq. (2) implies that for purely ionizing or purely recombining phase plasmas, the ratio of the intensities of two lines from the same ionization stage will scale roughly as $I_{ki}/I_{pq} \propto n_k/n_p \sim \exp((E_p - E_k)/k_B T_e)$, where k and p label the upper energy levels and i and q label the

lower levels of the respective atomic transitions. Thus, if $E_k > E_p$, I_{ki}/I_{pq} will be an increasing function of the electron temperature, and the line ratio can be used as a qualitative diagnostic for changes in T_e , which may be made quantitative if a sufficiently accurate model for $\alpha_k^j(n_e, T_e)$ and $\beta_k^j(n_e, T_e)$ exists.

However, if the plasma transitions from a predominantly ionizing phase to a predominantly recombining phase, it is no longer possible to compare line ratios and infer relative T_e values. This point is vividly illustrated in Fig. 10(a), which shows the measured $[\text{Ar I } 703.0 \text{ nm}]/[\text{Ar I } 696.5 \text{ nm}]$ line ratio during discharges with the magnetic field coils turned

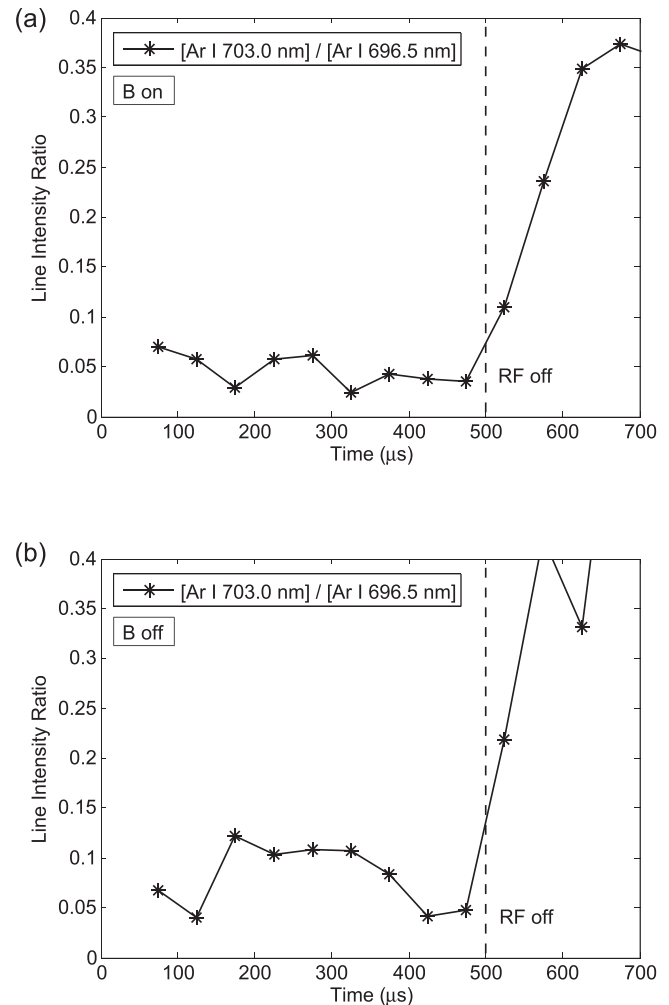


FIG. 10. $[\text{Ar I } 703.0 \text{ nm}]/[\text{Ar I } 696.5 \text{ nm}]$ line intensity ratio during discharges with the RF amplifier pulsed for $500 \mu\text{s}$ and the bias and solenoid magnetic fields either on (a) or off (b). The data were averaged over 20 shots for each line and binned in $25 \mu\text{s}$ intervals.

on and the RF power on for $500 \mu\text{s}$. The upper level energy of the 703.0 nm line is higher than that of the 696.5 nm line by 1.52 eV , so this line ratio would normally be an increasing function of T_e , sensitive to temperature in the $T_e = 1 - 3 \text{ eV}$ regime relevant to our experiment. Given that T_e is known to fall rapidly after RF turn-off,^{3,6} the dramatic increase in the measured line ratio after $t = 500 \mu\text{s}$ seems surprising. Similar trends were also observed for other line ratios nominally expected to decrease with decreasing T_e , including $[\text{Ar I } 735.3 \text{ nm}]/[\text{Ar I } 738.4 \text{ nm}]$ and $[\text{Ar I } 687.1 \text{ nm}]/[\text{Ar I } 763.5 \text{ nm}]$. The observed behavior may be understood by realizing that the plasma transitioned to a recombining phase after RF turn-off. Three-body recombination occurs mostly into highly excited states, causing recombining phase plasmas to have enhanced population densities in the upper atomic energy levels compared to ionizing phase plasmas,²⁸ even if T_e is very low. These enhanced upper level populations lead to the characteristic brightness of the afterglow that was seen in Fig. 2 and in many other discharges.^{4,29}

The rise in visible emission during the afterglow phase explains why the expanding cone of plasma in the magnetized RF discharges was visible in camera images during the $200\text{--}400 \mu\text{s}$ interval when the RF power was turned off at $t = 200 \mu\text{s}$ (Fig. 5), but not when it was left on until $t = 400 \mu\text{s}$ (Fig. 6), even though I_{sat} measured by the Langmuir probe (Fig. 8) was similar in both cases. The line ratios in Fig. 10 are also helpful for understanding the differences between Figs. 6 and 7. During the $200\text{--}400 \mu\text{s}$ interval, the $[\text{Ar I } 703.0 \text{ nm}]/[\text{Ar I } 696.5 \text{ nm}]$ ratio was twice as high for discharges with $B = 0$ (Fig. 10(b)) than for discharges with finite B (Fig. 10(a)). The enhanced $6s$ level population in the $B = 0$ case helps to explain why the expanding plasma, known to be present in both cases from the probe data in Fig. 8, could be seen in Fig. 7 but not in Fig. 6—plasmas with high population densities in upper atomic energy levels have enhanced visible and IR brightness. We hypothesize that in the case with $B = 0$, the cloud of plasma in the chamber was poorly coupled to the power source because hot electrons coming from the antenna region were not well confined and most were lost to the walls of the tube. Thus, this plasma was closer to being in the recombining phase than the plasma expanding along a confining field.

As noted in Sec. IV, the mean free path for reabsorption of 696.5 nm emission was on the order of a few cm, so the intensity I_{ki} of this line and others may not have been exactly proportional to the line-averaged population density n_k of the relevant upper energy level. However, this effect should not alter the basic qualitative conclusions drawn from the data in this section. Specifically, we have shown that the brightness of the expanding RF plasma did not scale with the ion density but instead was enhanced at certain locations and times due to recombination populating high-lying Ar I states that subsequently decayed through spontaneous emission.

At first glance, the conclusion that the camera images were deceptive may seem to invalidate the pressure-measurement method presented in Sec. IV, which relied on detecting visible and IR emission from the antenna region. However, it was not required to have emissivity proportional

to plasma density in order to apply this technique. The total brightness integrated over all wavelengths detected by the photodiode was a complex function of n_e , T_e , and n_{Ar} , so if two discharges had precisely the same time-varying emission pattern, as illustrated in Fig. 3, then it was reasonable to conclude that n_{Ar} in the emitting region must have been the same in both cases.

VI. DENSITY RISE IN THE AFTERGLOW

In the images taken of discharges with a $400 \mu\text{s}$ RF pulse (Figs. 6 and 7), a new cloud of plasma appears to emerge from the discharge tube and expand into the chamber after RF power turn-off. It is likely that electrons cascading to the ground state following recombination were at least partially responsible for the increased brightness at $t > 400 \mu\text{s}$; however, in the magnetized experiments, the ion saturation current at $z = 6 \text{ cm}$ also increased at this time, as seen in Fig. 8. If the time of RF turn-off was varied, there was a corresponding shift in the timing of the secondary I_{sat} peak in the afterglow, as shown in Fig. 11.

Analysis of the full Langmuir probe IV curve (feasible in the afterglow because there was no RF present) confirmed that the I_{sat} increase was due to a rise in the local ion density, rather than an electron temperature increase. Fig. 12 shows that T_e fell rapidly to $< 0.5 \text{ eV}$ after RF turn-off. Meanwhile, n_i increased by at least 10^{18} m^{-3} at both $z = 0.0 \text{ cm}$ and $z = 6.0 \text{ cm}$ (recall that the density measured by the probe may have been underestimated due to ion-neutral collisions), but the ratio of the peak n_i in the afterglow to its value before RF turn-off was much higher at $z = 6.0 \text{ cm}$. Inside the discharge tube near the antenna (at $z = -5.7 \text{ cm}$), I_{sat} decreased monotonically after RF turn-off (see Ref. 25, Figure 5.9)).

Despite the correspondence that was established in Sec. IV between the visible/IR light emission in the discharge tube for experiments with the fast gas valve used and with a uniform backfill, the downstream density evolution was dramatically different, as shown in Fig. 13. This is not surprising, given that the fast gas valve produced much lower

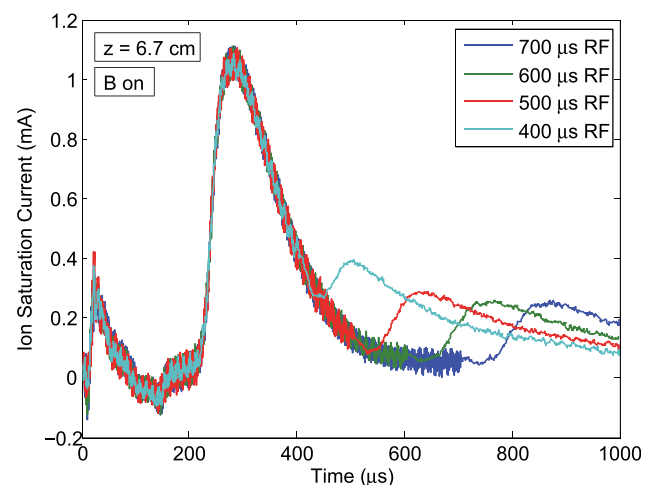


FIG. 11. Ion saturation current (measured with $V_{\text{probe}} = -13.8 \text{ V}$) at $z = 6.7 \text{ cm}$ for discharges with the RF amplifier turned off at four different times. The bias field coil and solenoid were turned on.

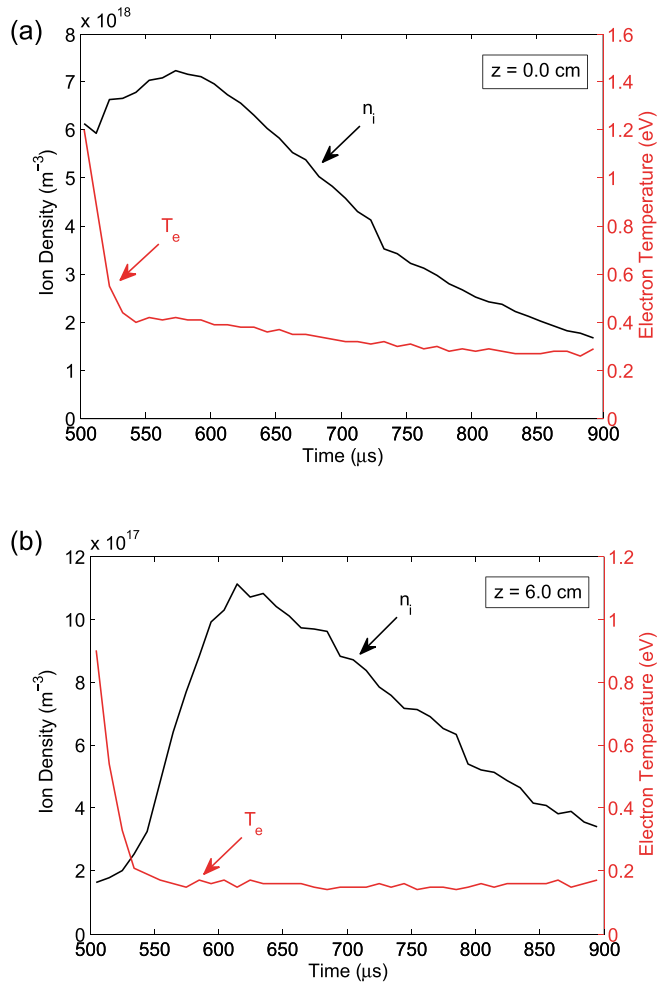


FIG. 12. $n_i(t)$ and $T_e(t)$ at $z = 0.0 \text{ cm}$ (a) and $z = 6.0 \text{ cm}$ (b) during the afterglow, measured by analyzing the full Langmuir probe I-V curve. The magnetic field coils were used, and the RF power was turned off at $t = 500 \mu\text{s}$.

P_{Ar} out in the main chamber than in the discharge tube due to radial expansion of the gas emerging from the tube. Plasma density increases of various magnitudes were observed after RF turn off for a range of gas capacitor bank voltages (Fig. 13(a)), but no afterglow density rise was seen in experiments with uniform P_{Ar} (Fig. 13(b)), except in cases in which the density at the probe location had not yet reached its initial peak when the power was turned off. Apparently, the nonuniform pressure distribution set up by the fast gas valve was critical for enabling the phenomenon to occur.

In principle, the density increase in the afterglow could have occurred either because new ions were created after RF turn-off or because plasma was confined deep in the discharge tube during the main discharge period and then released when the power was turned off. Confinement via the ponderomotive force³⁰ was considered as a possible explanation, but this effect was ruled out when no clear peaks in the RF electric field amplitude were found in an axial Langmuir probe scan. Given that T_e was below 0.5 eV , the electron impact ionization rate in the afterglow was negligible. However, ionization can also occur as a result of a collision between two excited neutral atoms if the sum of

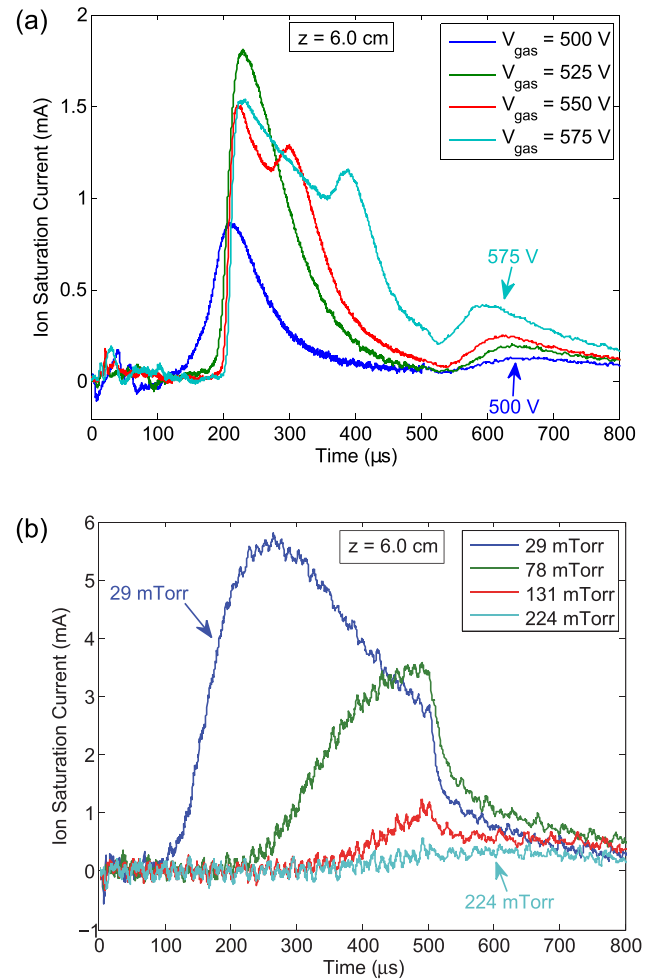
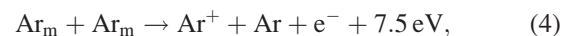


FIG. 13. (a) Ion saturation current (measured with $V_{probe} = -15.4 \text{ V}$) at $z = 6.0 \text{ cm}$ during experiments with the fast gas valve used. (b) $I_{sat}(t)$ (measured with $V_{probe} = -25.0 \text{ V}$) at $z = 6.0 \text{ cm}$ during experiments with a uniform argon gas pressure in the chamber. In both cases, the RF power was turned on from $t = 0$ – $500 \mu\text{s}$, and the bias magnetic field was applied ($V_{bias} = 80 \text{ V}$, $V_{sol} = 0 \text{ V}$).

their energies above the ground state exceeds the ionization energy. The most common example of this process, which is known as “energy pooling,” is metastable-metastable ionization



where the excess energy is carried away by the free electron. Electron-impact ionization dominates over pooling ionization as long as the electrons are being heated to several eV by an external power source; however, energy pooling can continue to produce new ions even after the power source has been turned off, thanks to the long-lived nature of metastables. Furthermore, the diffusive loss rate of ions, which is proportional to T_e , falls dramatically in the afterglow, so it is possible for the pooling ionization rate to temporarily exceed the loss rate, in which case n_i grows.

Afterglow density increases have been observed and attributed to pooling ionization in a number of other RF, microwave, and DC glow discharges at 0.1 – 3 Torr , most commonly in helium discharges^{16,17} but also with argon¹⁸ and neon.¹⁶ In our experiment, the effect was present when

operating with any of these three gases (see Ref. 25; Figure 5.11).

Pooling ionization in an argon discharge should be inhibited by the addition of hydrogen,³¹ which tends to depopulate the argon excited states (the rate coefficients for de-excitation of an argon metastable by collisions with an H₂ molecule or H atom are $K_{H_2} \approx 10^{-16}$ m³/s and $K_H \approx 2 \times 10^{-16}$ m³/s, respectively,³² so with a hydrogen partial pressure of 30 mTorr, the mean lifetime of an argon metastable is ≤ 10 μ s). Fig. 14(a) demonstrates that adding hydrogen in our experiment caused the afterglow density peak to disappear for $p_{H_2} = 40$ mTorr and above. On the other hand, in similar experiments in which the chamber was filled uniformly with argon at 0–40 mTorr before additional argon gas was supplied to the discharge tube using the fast gas valve (Fig. 14(b)), the afterglow density increase persisted. This result shows that the mere presence of a uniform gas backfill prior to fast argon gas injection was not the reason for the disappearance of the afterglow density increase in Fig. 14(a); rather, it was caused by the unique

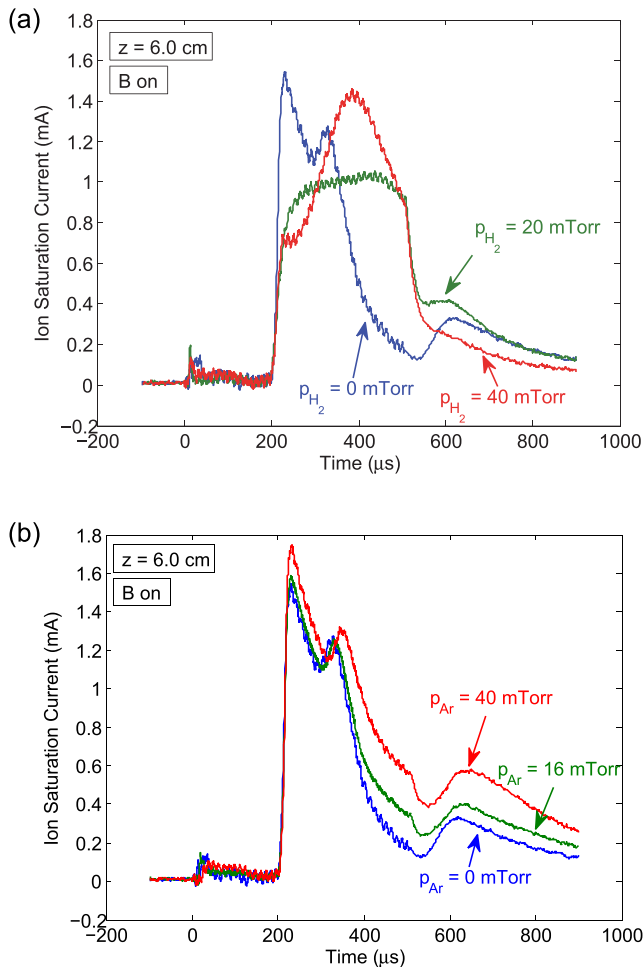


FIG. 14. (a) Ion saturation current (measured with $V_{probe} = -15.4$ V) at $z = 6.0$ cm during experiments with a uniform hydrogen backfill and argon also supplied to the RF discharge tube using the fast gas valve ($V_{gas} = 550$ V). (b) I_{sat} . at $z = 6.0$ cm during experiments with a uniform argon backfill and additional argon supplied using the fast gas valve. In both cases, the RF power was turned on from $t = 0$ –500 μ s, and the bias magnetic field was applied ($V_{bias} = 80$ V, $V_{sol.} = 0$ V). The blue curves on each plot show the control case with no initial uniform gas backfill.

metastable-depopulating property of hydrogen impurities in an argon discharge. Fig. 14 thus supports the hypothesis that pooling ionization played an important role.

Taking the cross section for metastable-metastable ionization to be $\sigma_{mm,iz.} = 1.35 \times 10^{-17}$ m² (Ref. 33) and assuming a typical relative velocity $v_r = 500$ m/s between the colliding atoms, the ionization rate coefficient was $K_{mm,iz.} = \sigma_{mm,iz.} v_r \approx 7 \times 10^{-15}$ m³/s, so a metastable population density $n_m = \sqrt{\dot{n}_i / K_{mm,iz.}} \sim 10^{18}$ m⁻³ was needed to account for the $\dot{n}_i \sim 10^{22}$ m⁻³/s measured in Fig. 12. On the other hand, given that two metastables are destroyed in every pooling ionization reaction, an initial population density $n_m \geq 2 \times 10^{18}$ m⁻³ was required in order to achieve $\Delta n_i \sim 10^{18}$ m⁻³ as in Fig. 12. These are plausible metastable population densities.

The metastable states were also depopulated by electron-impact transitions to the 4s resonant state followed by radiative decay to the ground state.³⁴ The rate coefficient for the metastable-to-resonant transition is $K_{mr} \approx 2 \times 10^{-13}$ m³/s, approximately independent of T_e above 0.2 eV,^{35,36} which implies that when the electron density in the afterglow was $n_e \approx 5 \times 10^{17}$ m⁻³, the mean lifetime for metastables was $\nu_{mr}^{-1} = (K_{mr} n_e)^{-1} \approx 10$ μ s. This observation appears to be problematic, given that the ion density rose over a period of ~ 100 μ s in the afterglow (Figs. 11 and 12) and few new metastables were created by electron impact excitation during this period. However, the re-absorption mean free path for photons created by resonant-to-ground state transitions was short—for example, at $n_{Ar} = 3 \times 10^{21}$ m⁻³ and $T_{gas} = 500$ K, Eq. (1) gives $l_{mfp} = (n_{Ar} \sigma_{\lambda_0})^{-1} \approx 4$ μ m for the Ar I 104.8 nm line—so the resonant level population density n_r may have remained high enough in the afterglow for the metastable levels to be re-populated by electron impact resonant-to-metastable transitions, increasing the effective lifetime. Furthermore, resonant-resonant and resonant-metastable energy pooling reactions would have contributed to the increase in ion density.

No other plausible mechanism has been identified for creating a sufficient number of new ions after RF turn-off, so pooling ionization remains the leading candidate to explain the afterglow density rise in our discharge. However, the question cannot be considered fully resolved. Direct measurements of the time-dependent population densities of metastables and other Ar I excited states using laser absorption spectroscopy would be extremely valuable for confirming the dominant ionization process and also for helping to understand why a significant afterglow density rise was only observed when a magnetic field was present and the fast gas valve was used.

VII. CONCLUSION

We have described several notable features of high-density inductively coupled argon plasmas expanding into a large chamber. A correspondence was established between the time-dependent visible light emission from discharges fed by a pulsed fast gas valve and discharges created with a uniform gas fill, enabling the pressure in the discharge tube in the former case to be inferred. The visible brightness of the expanding plasma was shown to be poorly correlated with the plasma density; this result was interpreted in light of

the relative argon excited state populations and the distinction between ionizing and recombining phase plasmas. Finally, the downstream ion density in magnetized discharges with nonuniform neutral gas density increased by $\sim 10^{18} \text{ m}^{-3}$ after RF turn-off. As part of the effort to understand these phenomena more completely, detailed numerical modeling of the discharges has been carried out;⁶ thus far the models have been successful in predicting the properties of pulsed plasmas formed at pressures below 100 mTorr, but they cannot yet accurately describe the behavior at higher pressures.

ACKNOWLEDGMENTS

This material is based upon work supported by the U.S. Department of Energy Office of Science, Office of Fusion Energy Sciences under Award Nos. DE-FG02-04ER54755 and DE-SC0010471 and by the National Science Foundation under Award No. 1059519. V. H. Chaplin acknowledges support by the ORISE Fusion Energy Sciences Graduate Fellowship.

- ¹M. A. Lieberman and A. J. Lichtenberg, *Principles of Plasma Discharges and Materials Processing*, 2nd ed. (Wiley-Interscience, Hoboken, NJ, 2005).
- ²P. Belenguer, M. Ganciu, P. Guillot, and T. Nelis, *Spectrochim. Acta Part B* **64**, 623 (2009).
- ³S. Ashida, C. Lee, and M. A. Lieberman, *J. Vac. Sci. Technol. A* **13**(5), 2498 (1995).
- ⁴A. Bogaerts, *J. Anal. At. Spectrom.* **22**, 502 (2007).
- ⁵S. C. Hsu and P. M. Bellan, *Phys. Plasmas* **12**, 032103 (2005).
- ⁶V. H. Chaplin and P. M. Bellan, *J. Appl. Phys.* **118**, 243303 (2015).
- ⁷A. L. Moser, "Dynamics of magnetically driven plasma jets: An instability of an instability, gas cloud impacts, shocks, and other deformations," Ph.D. thesis (California Institute of Technology, 2012).
- ⁸S. C. Hsu and P. M. Bellan, *IEEE Trans. Plasma Sci.* **30**(1), 10 (2002).
- ⁹A. D. Light, S. C. Thakur, C. Brandt, Y. Sechrest, G. R. Tynan, and T. Munsat, *Phys. Plasmas* **20**, 082120 (2013).
- ¹⁰B. A. Jorns and R. R. Hofer, *Phys. Plasmas* **21**, 053512 (2014).

- ¹¹S. J. Zweben, R. J. Maqueda, D. P. Stotler, A. Keesee, J. Boedo, C. E. Bush, S. M. Kaye, B. LeBlanc, J. L. Lowrance, V. J. Mastrocola, R. Maingi, N. Nishino, G. Renda, D. W. Swain, J. B. Wilgen, and the NSTX Team, *Nucl. Fusion* **44**, 134 (2004).
- ¹²D. M. Goebel and I. Katz, *Fundamentals of Electric Propulsion: Ion and Hall Thrusters* (John Wiley & Sons, Inc., Hoboken, NJ, 2008).
- ¹³K. K. Jameson, D. M. Goebel, R. R. Hofer, and R. M. Watkins, in *30th International Electric Propulsion Conference* (Florence, Italy, 2007).
- ¹⁴V. H. Chaplin and P. M. Bellan, *Rev. Sci. Instrum.* **86**, 073506 (2015).
- ¹⁵T. Fujimoto, *J. Phys. Soc. Japan* **47**(1), 265 (1979).
- ¹⁶M. A. Biondi, *Phys. Rev.* **88**(3), 660 (1952).
- ¹⁷K. E. Greenberg and G. A. Hebner, *J. Appl. Phys.* **73**(12), 8126 (1993).
- ¹⁸Y. Ohtsu, K. Shimizu, and H. Fujita, *Electr. Eng. Jpn.* **135**(2), 26 (2001).
- ¹⁹L. J. Overzet and J. Kleber, *Plasma Sources Sci. Technol.* **7**, 512 (1998).
- ²⁰T. Shoji, Y. Sakawa, S. Nakazawa, K. Kadota, and T. Sato, *Plasma Sources Sci. Technol.* **2**, 5 (1993).
- ²¹L. J. Overzet and M. B. Hopkins, *J. Appl. Phys.* **74**(7), 4323 (1993).
- ²²P. M. Bellan, *Rev. Sci. Instrum.* **73**, 2900 (2002).
- ²³G. B. Rybicki and A. P. Lightman, *Radiative Processes in Astrophysics*, 2nd edn. (Wiley-VCH, Germany, 2004).
- ²⁴A. Kramida, Y. Ralchenko, J. Reader, and NIST ASD Team, NIST Atomic Spectra Database (ver. 5.1), National Institute of Standards and Technology, Gaithersburg, MD, 2013, see <http://physics.nist.gov/asd> (last accessed January 6 (2014)).
- ²⁵V. H. Chaplin, "Battery-powered RF pre-ionization system for the Caltech magnetohydrodynamically-driven jet experiment: RF discharge properties and MHD-driven jet dynamics," Ph.D. thesis (California Institute of Technology, 2015).
- ²⁶A. C. Hossack, T. Firman, T. R. Jarboe, J. R. Prager, B. S. Victor, J. S. Wrobel, and T. Ziemba, *Rev. Sci. Instrum.* **84**, 103506 (2013).
- ²⁷P. M. Bellan, *Fundamentals of Plasma Physics* (Cambridge University Press, New York, 2006).
- ²⁸A. Hirabayashi, Y. Nambu, M. Hasuo, and T. Fujimoto, *Phys. Rev. A* **37**(1), 77 (1988).
- ²⁹G. P. Jackson and F. L. King, *Spectrochim. Acta Part B* **58**, 1417 (2003).
- ³⁰B. M. Lamb, G. Dimonte, and G. J. Morales, *Phys. Fluids* **27**, 1401 (1984).
- ³¹A. Bogaerts, *J. Anal. At. Spectrom.* **17**, 768 (2002).
- ³²A. Bogaerts and R. Gijbels, *J. Anal. At. Spectrom.* **15**, 441 (2000).
- ³³T. Okada and M. Sugawara, *Jpn. J. Appl. Phys., Part 1* **35**, 4535 (1996).
- ³⁴Y. Celik, T. V. Tsankov, M. Aramaki, S. Yoshimura, D. Luggenhölscher, and U. Czarnetzki, *Phys. Rev. E* **85**, 056401 (2012).
- ³⁵E. A. Andreev and A. E. Bodrov, *Chem. Phys. Lett.* **109**(5), 450 (1984).
- ³⁶C. M. Ferreira, J. Loureiro, and A. Ricard, *J. Appl. Phys.* **57**(1), 82 (1985).